Article

Localization of lattice dynamics in low-angle twisted bilayer graphene

https://doi.org/10.1038/s41586-021-03252-5

Received: 15 June 2020

Accepted: 4 December 2020

Published online: 17 February 2021

Check for updates

Andreij C. Gadelha[1], Douglas A. A. Ohlberg[1], Cassiano Rabelo[2], Eliel G. S. Neto[3], Thiago L. Vasconcelos[4], João L. Campos[1], Jessica S. Lemos[1], Vinícius Ornelas[1], Daniel Miranda[1], Rafael Nadas[1], Fabiano C. Santana[1], Kenji Watanabe[5], Takashi Taniguchi[5], Benoit van Troeye[6], Michael Lamparski[6], Vincent Meunier[6]✉, Viet-Hung Nguyen[7], Dawid Paszko[7], Jean-Christophe Charlier[7], Leonardo C. Campos[1], Luiz G. Cançado[1], Gilberto Medeiros-Ribeiro[8] & Ado Jorio[1,2]✉

Twisted bilayer graphene is created by slightly rotating the two crystal networks in bilayer graphene with respect to each other. For small twist angles, the material undergoes a self-organized lattice reconstruction, leading to the formation of a periodically repeated domain[1–3]. The resulting superlattice modulates the vibrational[3,4] and electronic[5,6] structures within the material, leading to changes in the behaviour of electron–phonon coupling[7,8] and to the observation of strong correlations and superconductivity[9]. However, accessing these modulations and understanding the related effects are challenging, because the modulations are too small for experimental techniques to accurately resolve the relevant energy levels and too large for theoretical models to properly describe the localized effects. Here we report hyperspectral optical images, generated by a nano-Raman spectroscope[10], of the crystal superlattice in reconstructed (low-angle) twisted bilayer graphene. Observations of the crystallographic structure with visible light are made possible by the nano-Raman technique, which reveals the localization of lattice dynamics, with the presence of strain solitons and topological points[1] causing detectable spectral variations. The results are rationalized by an atomistic model that enables evaluation of the local density of the electronic and vibrational states of the superlattice. This evaluation highlights the relevance of solitons and topological points for the vibrational and electronic properties of the structures, particularly for small twist angles. Our results are an important step towards understanding phonon-related effects at atomic and nanometric scales, such as Jahn–Teller effects[11] and electronic Cooper pairing[12–14], and may help to improve device characterization[15] in the context of the rapidly developing field of twistronics[16].

The lattice dynamics of graphite has been widely studied because of the potential to engineer the thermal and electrical properties of this semi-metal[17]. Bilayer graphene in the Bernal stacking (or AB stacking) represents the basic two-dimensional unit which with to build three-dimensional graphite. It has recently gained attention because of its rich structural and electronic behaviour when arranged with a small relative twist angle θ between the two layers. Below a threshold twist angle $\theta_c \approx 1°$, twisted bilayer graphene (TBG) undergoes an energetically favourable atomic reconstruction, entering the soliton regime for $\theta < \theta_c$ (refs. [3,18]). This equilibrium configuration has alternating AB and BA triangular stacking domains separated by shear solitons, which represent saddle points of the van der Waals energy landscape[1] in the hexagonal network[1,18], with AA-stacked topological regions at the vertices of the triangular areas (Fig. 1a). This reconstructed twisted bilayer graphene (rTBG) is a new material system, in which emerging local phenomena related to electronic and phononic reconstructions and to morphology rearrangement[6,18] are yet to be fully understood.

Nano-Raman hyperspectral imaging

Raman spectroscopy—based on the inelastic scattering of light—is a key experimental technique for studying the vibrational structure of graphite-related systems[19]. It is also important for studying low-dimensional structures[20,21], for which inelastic neutron and X-ray scattering are difficult to use. However, to visualize the detailed structure of rTBG, a nano-Raman spectroscope—capable of resolving

[1]Physics Department, Universidade Federal de Minas Gerais, Belo Horizonte, Brazil. [2]Electrical Engineering Graduate Program, Universidade Federal de Minas Gerais, Belo Horizonte, Brazil. [3]Physics Institute, Universidade Federal da Bahia, Campus Universitário de Ondina, Salvador, Brazil. [4]Divisão de Metrologia de Materiais, Inmetro, Duque de Caxias, Brazil. [5]National Institute for Materials Science, Ibaraki, Japan. [6]Department of Physics, Applied Physics, and Astronomy, Jonsson Rowland Science Center, Troy, NY, USA. [7]Institute of Condensed Matter and Nanosciences, Université Catholique de Louvain, Louvain-la-Neuve, Belgium. [8]Computer Science Department, Universidade Federal de Minas Gerais, Belo Horizonte, Brazil. ✉e-mail: meuniv@rpi.edu; adojorio@fisica.ufmg.br

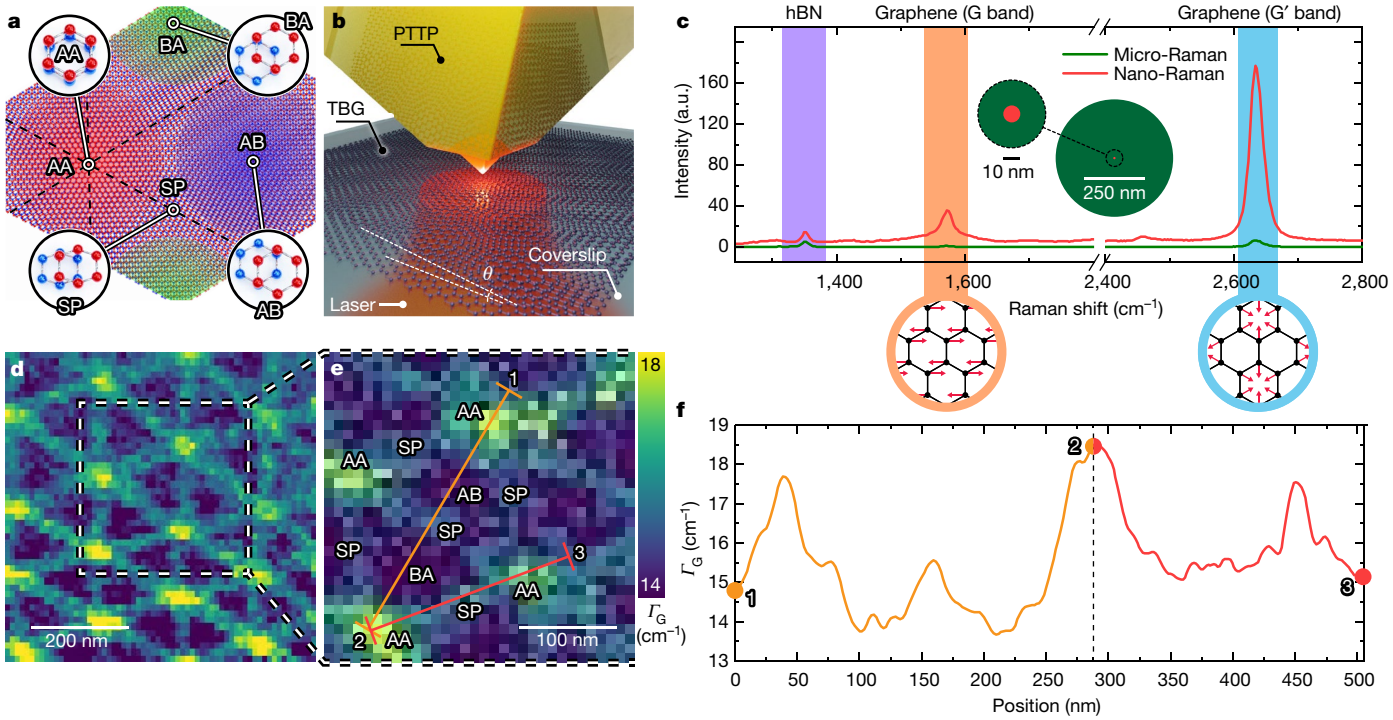

Fig. 1 | Nano-Raman spectral imaging of a crystallographic superlattice in rTBG. **a**, Schematics of neighbouring AB- and BA-stacked domains, strain solitons (SP) and topological points (AA). **b**, Schematics of the plasmon-tunable tip pyramid (PTTP) nano-antenna responsible for the enhancement of the Raman signal in a nanometric area, in the tip-enhanced Raman spectroscopy configuration. **c**, Comparison between micro-Raman (green) and nano-Raman (red) spectra in the sample (an enlarged version of the green spectrum is shown in Extended Data Fig. 1). Green and red circles (main inset) indicate the different illumination areas. The G and G′ vibrational modes are depicted by the red arrows (orange and blue bands, bottom insets), as well as the peak from the hexagonal boron nitride (hBN) substrate (purple band). The G′ band is also named '2D' in the literature. **d**, Crystallographic hyperspectral image of rTBG based on the G′-band nano-Raman intensity. **e**, Close-up of the boxed region in **d**, built on the basis of the G-band nano-Raman linewidth Γ_G. **f**, Line profile for Γ_G along the high-symmetry directions shown by the orange and red lines in **e**. The data are averaged over the pixels delimited by the ending bars of those lines. a.u., arbitrary units.

optical information below the diffraction limit of light (Fig. 1b, c)—is necessary[10]. Figure 1d–f shows nano-Raman imaging of solitonic arrangements in rTBG with superlattice periodicity of $L_M = 160 \pm 30$ nm, which corresponds to $\theta = 0.09° \pm 0.02°$, using $L_M = a_0/2\sin(\theta/2)$ and a graphene lattice parameter of $a_0 = 0.245 \pm 0.001$ nm. The specific nano-antenna used in our nano-Raman setup, a plasmon-tunable tip pyramid[22] shown schematically in Fig. 1b, is crucial for the acquisition of the images shown in Fig. 1d, e. It yields a local signal enhancement of roughly 3×10^3, generating a nano-Raman signal so intense that the micro-Raman response from the micrometre-sized illumination area becomes negligible (Fig. 1c). The nano-Raman images are obtained at ambient conditions over regions of the bilayer that appear atomically flat and featureless in the surface topology images obtained simultaneously by the nano-antenna, which also functions as an atomic force microscope probe (see Methods for details of sample preparation, characterization and optical setup).

The particular configuration shown in Fig. 1d was observed previously using transmission electron microscopy[1,3,4] and nano-infrared spectroscopy[23]. In these studies, the solitonic structure and soliton interceptions are attributed to shear strain solitons and topological AA points, respectively, on the basis of the similarity between the observed superlattices and theoretical expectations for rTBG at low twist angles (Fig. 1a). Here, the superlattice imaging is related directly to the distribution of local vibrational states and the electronic structure of rTBG, because the nano-Raman spectroscopy probes the local vibration of the atomic lattice directly. The main Raman spectral signatures in graphene are due to the stretching of the C–C bonds (conventionally named the G band, appearing at 1,584 cm^{-1}) and the breathing motion of the hexagonal carbon rings (with the two-phonon symmetry-allowed scattering appearing at 2,640 cm^{-1}, named G′ band; Fig. 1c). Figure 1d shows a hyperspectral image based on the intensity of the Raman G′ band of rTBG; Fig. 1e shows a close-up of a region of Fig. 1d and is built on the basis of the linewidth Γ_G of the Raman G band. In these images, the datasets are plotted in their raw forms, without any statistical treatment or data filtering.

Phonon localization

Not only are the specific vibrational modes for the Raman G and G′ bands (Fig. 1c, bottom insets) different, but the scattering mechanisms responsible for these Raman features[20,21] differ as well. The G band is a first-order Raman-active mode related to the doubly-degenerate high-frequency optical phonon branch in graphene at the centre of the Brillouin zone (Γ point; Fig. 2a, red lines). Whereas the Bernal-stacked bilayer graphene exhibits a single Raman-active phonon band, the rTBG exhibits a splitting of the vibrations in several branches[6], two of which are evident in the high-frequency branch at the Γ point. Previous models for TBG[7] cannot explain this splitting because the phonon branches result from atomic reconstruction with the emergence of topological solitons. In contrast to results reported previously, our methodology enables unfolding of the tens of thousands of phononic bands of the large rTBG unit cell into those of graphene. This capability makes it possible to monitor how the intrinsic phonon properties of graphene evolve when relaxing into the rTBG structure. We show an example of the resulting (unfolded) band structure in Fig. 2a for an rTBG (blue lines) with a twist angle of 0.987°. In addition, we show the local phonon density of states (DOS) around the lower-frequency (G_r^-) and higher-frequency (G_r^+) phonon branches (Fig. 2b, c, left). These results are also attributable to our fully atomistic model, which enables analysis of the localized projected phonon DOS in AA, AB–BA and

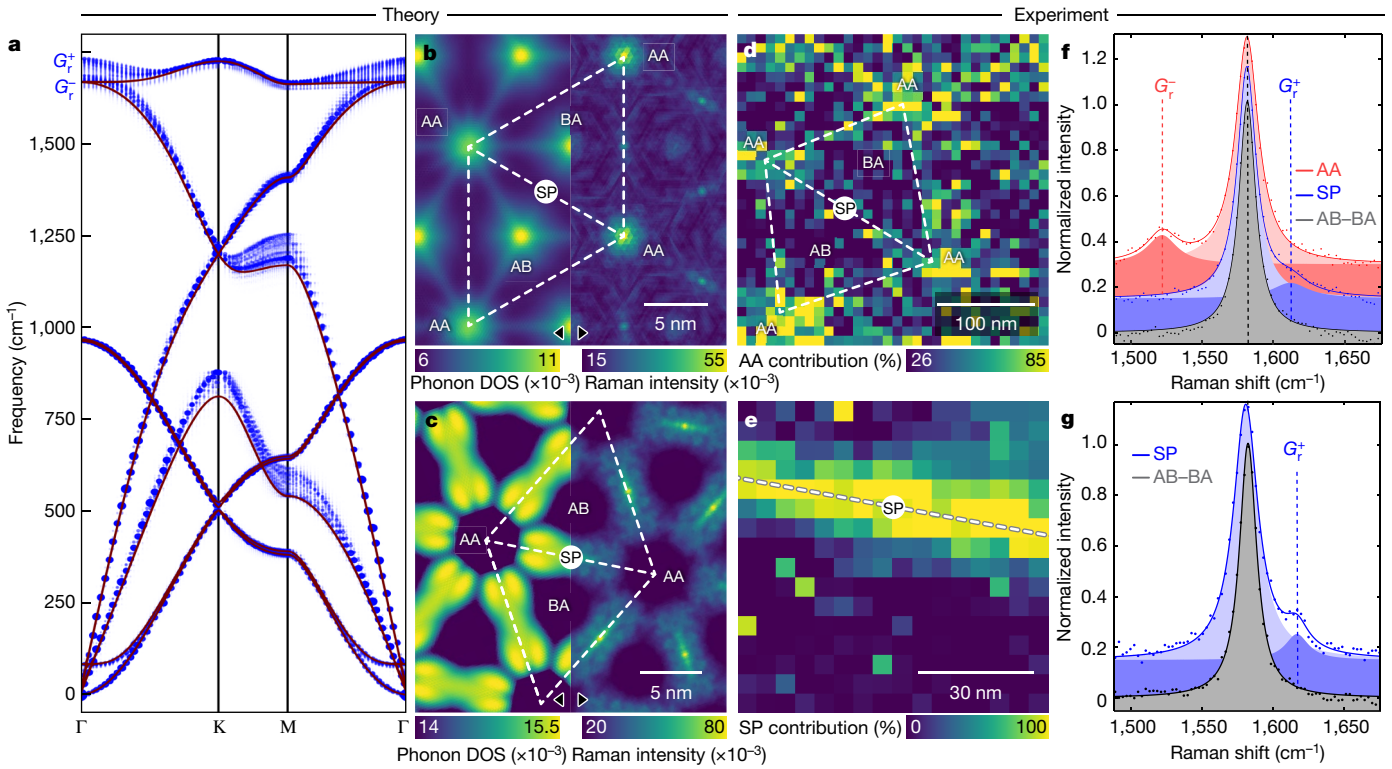

Fig. 2 | Phonon structure and the nano-Raman spectral signature. a, Theoretical phonon dispersion for Bernal AB-stacked bilayer graphene (red) and for rTBG (blue). The band structure for rTBG was obtained by unfolding the phonon bands of the small Brillouin zone of the superlattice onto the much larger Brillouin zone of graphene. The frequency degeneracy at the Γ point for the AB-stacked phonon (red) and lower-branch rTBG (blue) may be lifted by different electron–phonon interactions, which are not considered in these calculations. **b**, **c**, Theoretically predicted spatial distributions of the phonon DOS (left) and Raman intensity (right) for the lower-frequency (G_r^-; **b**) and higher-frequency (G_r^+; **c**) optical phonons at the Γ point. The images in **b** and **c** differ in size and position with respect to each other, for better comparison to **d** and **e**. **d**, **e**, Experimentally measured hyperspectral mapping of the AA (**d**) and SP (**e**) Raman spectra, as defined in **f** and **g** (the contribution indicates their respective spectral weight, as defined in Methods). **f**, **g**, Representative G-band spectra of AA, SP and AB–BA regions, obtained from the hyperspectra in **d** and **e**, respectively. The experimentally observed G_r^- and G_r^+ peaks are indicated. Data in **d** and **f** come from the same location as for Fig. 1c. Data for other rTBG samples are shown in Extended Data Fig. 2.

saddle-point (SP) stacking regions. These modes are therefore predicted to be localized in space, with the lower-frequency mode G_r^- appearing more strongly in the AA regions and at the very centre of the AB–BA domains and the higher-frequency mode G_r^+ appearing more strongly in the SP regions.

Close inspection of the experimental Raman data reveals two satellite peaks next to the G band, which appear above and below it and are also named G_r^+ and G_r^-, respectively (Fig. 2d–g). Remarkably, they are localized in space exactly as predicted by theory (Fig. 2b–e). The Raman intensity is not only defined by the phonon DOS, but also depends on the electron–phonon coupling. The absence of an experimental contribution from G_r^- at the centre of the AB–BA domains (compare Fig. 2b and Fig. 2d) is in agreement with the Raman intensities computed using the bond polarizability model[24] (Fig. 2b, c, right; Supplementary Information). The G band is reminiscent of the unfolded structure. It is partially contaminated by data from the Bernal-stacked region, owing to the limited resolution of the tip-enhanced Raman spectroscopy, but also exhibits local information, as clearly evidenced by the change in linewidth shown in Fig. 1e, f.

The theoretically predicted phonon localization, which cannot be accessed via the usual continuous models, is consistent with the experimental nano-Raman results of highly localized phonons in rTBG. Figure 2d, f shows data from the same location used in Fig. 1e; Fig. 2d shows the local contribution of the AA spectrum in Fig. 2f, and Fig. 2e is a higher-resolution image of a single soliton, to better demonstrate the localization of the SP spectra with the lower-intensity G_r^+ peak (Fig. 2g). This data processing relied on principal component analysis (Methods).

Electron localization

The Raman G′ band, used to obtain Fig. 1d, is also related to the high-frequency optical phonon branch in graphene, but away from the centre of the Brillouin zone, close to the K or K′ points[20,21,25]. Figure 3a, b illustrates nano-Raman spectra observed at an AB–BA region and at a SP region. We see no clear distinction between the spectral signatures of the soliton and AA regions. The spectrum shown in Fig. 3a is typical of a Bernal-stacked bilayer, with four Lorentzian peaks[26], thus confirming the AB stacking structure. The spectrum in Fig. 3b is different, displaying a unique SP–AA Raman signature. These spectral profiles were used to fit the G′ hyperspectra shown in Fig. 1. The spectral weights of the AB–BA and SP–AA spectra are plotted in Fig. 3c, d, clearly demonstrating the rTBG structure.

The G′ line shape is known to be sensitive to the electronic structure, because it is mediated in part by electron–phonon coupling[20,21,25]. Moreover, it depends on the number of Bernal-stacked layers[26] and on the twist angle[7]. Here, we show that in rTBG both the phonon structure and the electronic structure exhibit localization, as shown previously[18] and discussed in detail in Supplementary Information. Figure 3e–g illustrates how the electronic DOS in momentum space, at a fixed energy E_{DOS}, changes locally in a typical low-angle rTBG system ($\theta = 0.505°$). Other low-angle rTBG structures are investigated and discussed in more detail in Supplementary Information. We chose $E_{DOS} = -0.98$ eV, the energy of the valence electrons that are excited to the conduction band by our excitation laser (laser energy $E_L = 1.96$ eV; $|E_{DOS}| = E_L/2$). Therefore, consistent with the non-local effects due to the number

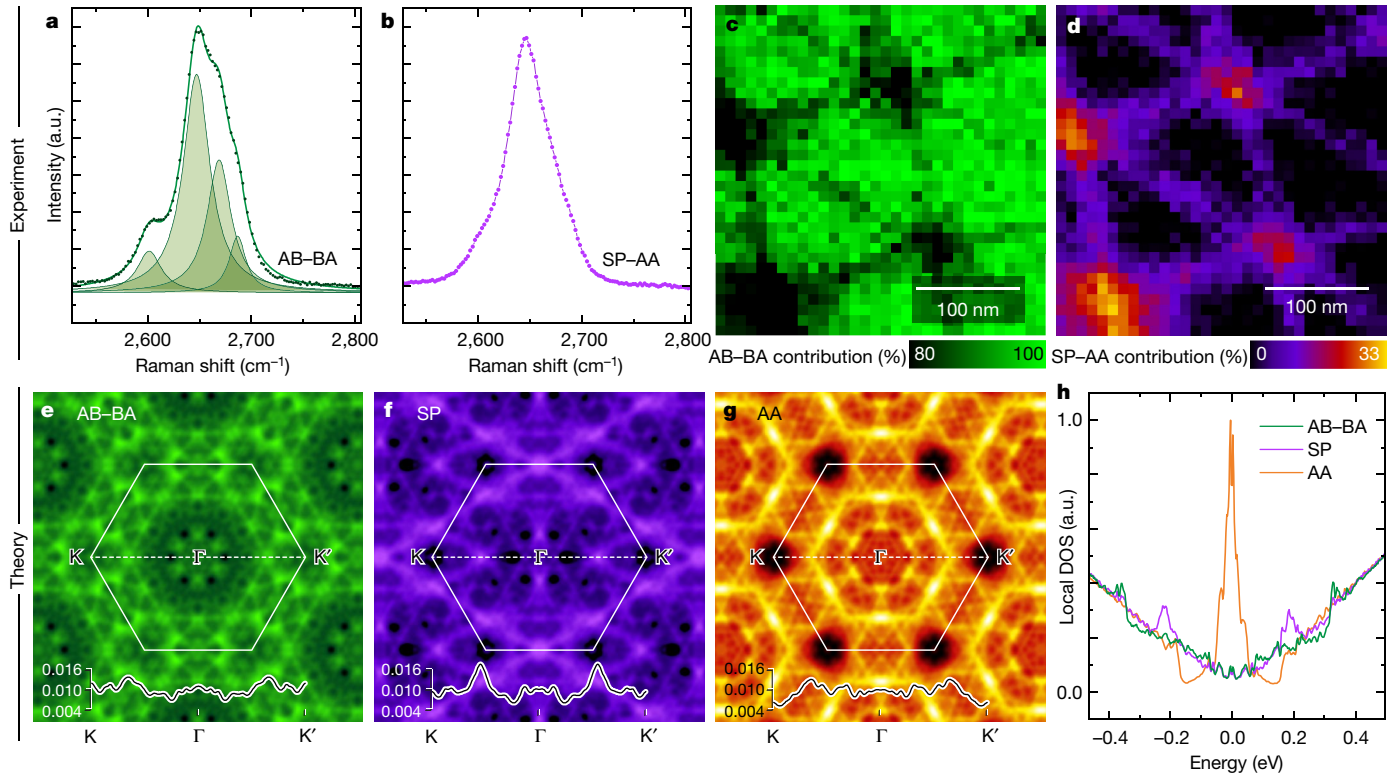

Fig. 3 | Nano-Raman spectral signatures (upper panels) and electronic structure (lower panels). a, **b**, Spectral Raman signatures of the AB–BA-stacked domains (**a**) and the SP–AA domains (**b**). **c**, **d**, Spectral weights for the AB–BA (**c**) and SP–AA (**d**) signatures, in rTBG real space (same location as for Fig. 1e). **e**–**g**, DOS (colour scale) at $E = -0.98$ eV, plotted in momentum space, for the AB–BA (**e**), SP (**f**) and AA (**g**) regions. Line traces of the DOS along the K–Γ–K′ direction are shown in the insets. The colours (green, purple and orange) relate to the real spatial locations in **c** and **d**. **h**, DOS as a function of energy near the Fermi level for the AB–BA, SP and AA regions.

of Bernal-stacked layers[26] or to the twist angle[7], the changes in the electronic structure of rTBG are qualitatively reflected locally in the spectral signature of the G′ band (Figs. 3a–d). However, a clear quantitative analysis requires further theoretical developments to address the electron–phonon coupling in these complex systems.

Although it is evident that strain has a role in the observed Raman frequencies and linewidths in rTBG, this time-independent perturbation alone cannot explain the observed results, as evidenced by the Γ_G line profile in Fig. 1f and by a joint analysis of the G and G′ features, based on what has been established in the literature (Extended Data Fig. 3)[27–29]. Aspects related to dynamic electron–phonon coupling, already shown to be very important in determining the phonon properties of graphene-related systems[30–33], including AB-stacked bilayer graphene[34], have to be taken into account. In this sense, changes in the local DOS for rTBG also take place near the Fermi level (Fig. 3h; see Supplementary Information for more details, including a localized joint DOS analysis), with further implications for the electron–phonon coupling and consequently the nano-Raman imaging. G-band phonons can be annihilated, generating an electron–hole pair. This mechanism decreases the overall lifetime of G-band phonons, thus broadening the G peak in the Raman spectrum[31,32,34]. A G-band phonon carries an energy of $\hbar\omega_G \approx 0.2$ eV ($\hbar$, reduced Planck constant; ω_G, G-band frequency). As a result, we expect that the presence of DOS peaks at ±0.2 eV for the SP region and at the Fermi level for the AA region in Fig. 3h, which are preserved even for smaller θ, will broaden the rTBG G band in the corresponding SP (purple) and AA (orange) regions. These predictions agree with the results shown in Fig. 1e, f, most notably in the AA regions, in which the G band is wider as a result of the DOS peak at the Fermi level (Fig. 3h). In addition, the widths of the G_r^- and G_r^+ peaks are 26–30 cm^{-1} and 30–32 cm^{-1}, respectively, with the G_r^- peak always slightly sharper (2–4 cm^{-1} narrower) than the G_r^+ peak. These values may provide insights into the real-space electron–phonon coupling, because the two modes are associated with regions with different stacking order.

Nano- and micro-Raman connection

To link the nano-Raman scattering experiments presented here with the usual micro-Raman spectroscopy characterization of TBG, in Fig. 4a we show the micro-Raman G and G′ spectra for different θ between 0.01° and 2.6°. For reference, we also plot in Fig. 4a the spectra for the Bernal bilayer graphene; Fig. 4b shows the full-width at half-maximum (FWHM) for the observed G band (Γ_G). An increase in Γ_G when decreasing the twist angle below $\theta = 5°$ was reported previously[35]. However, here we see evidence that Γ_G reaches a maximum near the magic angle ($\theta \approx 1.1°$)[9] and decreases for lower θ, approaching the reference Bernal AB stacking value of $\Gamma_G = 12$ cm^{-1} as $\theta \to 0$ (Fig. 4b). Considering the reconstruction regime for $\theta < 1.2°$ (ref. [18]), as θ decreases, the ratio between the areas of the AA–SP and AB–BA regions decreases and the TBG G band tends to the corresponding AB version (Fig. 4b). However, it is interesting to have found Γ_G as high as 19 cm^{-1} near the magic angle, consistent with the Γ_G observed at AA points in Fig. 1e, f. This value is higher than that of graphene at the charge neutrality point, where the electron–phonon coupling is maximum[31,32]. As already pointed out, Γ_G is affected by both strain and the time-dependent perturbations related to the electron–phonon coupling[34,36]. Our Γ_G results indicate a peak in the electron–phonon coupling near the magic angle, which provides evidence of a possible role for phonons in graphene superconductivity. However, the relation between Γ_G and the theoretical analysis of strain and local DOS-based electron–phonon coupling is only qualitative. Future temperature-dependent experiments to extract the contribution

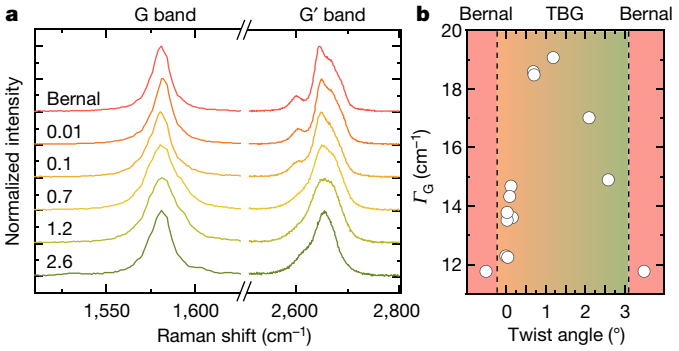

Fig. 4 | Micro-Raman spectral signature for TBG at different twist angles. **a**, G- and G′-band spectra for different θ (as labelled). The spectra are offset for clarity. The values of θ were measured using high-resolution scanning microwave impedance microscopy. The spectrum for Bernal stacking was measured for reference. **b**, FWHM (Γ_G) of the G peak for different θ (more information in Extended Data Fig. 4). The shading in **b** corresponds to the colouring of the lines in **a**.

from anharmonic effects (phonon–phonon interaction[37]) and low-temperature gate-doping experiments[31] to independently change the electron–phonon coupling may quantify the importance for Γ_G of electron–phonon coupling as opposed to other possible structural effects[5,6]. The results might differ from those of similar work on single-layer and AB-bilayer graphene[31,32,34], because in rTBG the electronic structure near the Fermi level is more complex and it may not be possible to switch off the coupling. Regardless, it may be possible to use the micro-Raman spectra to evaluate twist-angle disorder[15] in rTBG and to search regions close to the magic angle.

Concluding remarks

Our results provide information on how local lattice vibrations and electron–phonon coupling behave in systems characterized by a soliton network, such as rTBG. Our findings rely on developments in nano-Raman techniques and on computational and algorithmic developments that enable an accurate description of the localization of phononic properties at length scales relevant to experiments. Our findings shed light on the importance of changes in the local DOS for the fundamental properties of rTBG at angles small enough to support the formation of soliton domains. They provide a basis for understanding many-body effects and for determining the optical, mechanical, thermal and electronic properties common to graphene-related systems but unique in rTBG systems, owing to the localization. Future advances require rigorous evaluation of the elements of the electron–phonon coupling matrix. Given the size of the systems considered, these elements cannot be computed directly without further algorithmic and theoretical developments. In general, our work provides a tool for the study of twistronics[16] and of many quantum properties and exotic phenomena absent in pristine graphene, such as ferromagnetism[38], the anomalous quantum Hall effect[39] and large linear-in-temperature resistivity[40], and may be useful for characterizing devices[15].

Online content

Any methods, additional references, Nature Research reporting summaries, source data, extended data, supplementary information, acknowledgements, peer review information; details of author contributions and competing interests; and statements of data and code availability are available at https://doi.org/10.1038/s41586-021-03252-5.

1. Jonathan, S. et al. Strain solitons and topological defects in bilayer graphene. *Proc. Natl Acad. Sci. USA* **110**, 11256–11260 (2013).
2. Lin, X., Liu, D. & Tománek, D. Shear instability in twisted bilayer graphene. *Phys. Rev. B* **98**, 195432 (2018).
3. Yoo, H. et al. Atomic and electronic reconstruction at the van der Waals interface in twisted bilayer graphene. *Nat. Mater.* **18**, 448–453 (2019).
4. Jiang, L. et al. Soliton-dependent plasmon reflection at bilayer graphene domain walls. *Nat. Mater.* **15**, 840–844 (2016).
5. Cocemasov, A. I., Nika, D. L. & Balandin, A. A. Phonons in twisted bilayer graphene. *Phys. Rev. B* **88**, 035428 (2013).
6. Lamparski, M., Van Troeye, B. & Meunier, V. Soliton signature in the phonon spectrum of twisted bilayer graphene. *2D Mater.* **7**, 025050 (2020).
7. Jorio, A. & Cançado, L. G. Raman spectroscopy of twisted bilayer graphene. *Solid State Commun.* **175–176**, 3–12 (2013).
8. Eliel, G. S. N. et al. Intralayer and interlayer electron–phonon interactions in twisted graphene heterostructures. *Nat. Commun.* **9**, 1221 (2018).
9. Cao, Y. et al. Unconventional superconductivity in magic-angle graphene superlattices. *Nature* **556**, 43–50 (2018).
10. Shao, F. & Zenobi, R. Tip-enhanced Raman spectroscopy: principles, practice, and applications to nanospectroscopic imaging of 2D materials. *Anal. Bioanal. Chem.* **411**, 37–61 (2019).
11. Angeli, M., Tosatti, E. & Fabrizio, M. Valley Jahn-Teller effect in twisted bilayer graphene. *Phys. Rev. X* **9**, 041010 (2019).
12. Wu, F., MacDonald, A. H. & Martin, I. Theory of phonon-mediated superconductivity in twisted bilayer graphene. *Phys. Rev. Lett.* **121**, 257001 (2018).
13. Wu, F., Hwang, E. & Das Sarma, S. Phonon-induced giant linear-in-*T* resistivity in magic angle twisted bilayer graphene: ordinary strangeness and exotic superconductivity. *Phys. Rev. B* **99**, 165112 (2019).
14. Lian, B., Wang, Z. & Bernevig, A. B. Twisted bilayer graphene: a phonon-driven superconductor. *Phys. Rev. Lett.* **122**, 257002 (2019).
15. Uri, A. et al. Mapping the twist-angle disorder and Landau levels in magic-angle graphene. *Nature* **581**, 47–52 (2020).
16. Mele, E. J. Commensuration and interlayer coherence in twisted bilayer graphene. *Phys. Rev. B* **81**, 161405 (2010).
17. Yoshimori, A. & Kitano, Y. Theory of the lattice vibration of graphite. *J. Phys. Soc. Jpn* **11**, 352–361 (1956).
18. Gargiulo, F. & Yazyev, O. V. Structural and electronic transformation in low-angle twisted bilayer graphene. *2D Mater.* **5**, 015019 (2017).
19. Tuinstra, F. & Koenig, J. L. Raman spectrum of graphite. *J. Chem. Phys.* **53**, 1126–1130 (1970).
20. Dresselhaus, M. S., Jorio, A., Hofmann, M., Dresselhaus, G. & Saito, R. Perspectives on carbon nanotubes and graphene Raman spectroscopy. *Nano Lett.* **10**, 751–758 (2010).
21. Ferrari, A. C. & Basko, D. M. Raman spectroscopy as a versatile tool for studying the properties of graphene. *Nat. Nanotechnol.* **8**, 235–246 (2013).
22. Vasconcelos, T. L. et al. Plasmon-tunable tip pyramids: monopole nanoantennas for near-field scanning optical microscopy. *Adv. Opt. Mater.* **6**, 1800528 (2018).
23. Sunku, S. S. et al. Photonic crystals for nano-light in moiré graphene superlattices. *Science* **362**, 1153–1156 (2018).
24. Liang, L., Puretzky, A. A., Sumpter, B. G. & Meunier, V. Interlayer bond polarizability model for stacking-dependent low-frequency Raman scattering in layered materials. *Nanoscale* **9**, 15340–15355 (2017).
25. Thomsen, C. & Reich, S. Double resonant raman scattering in graphite. *Phys. Rev. Lett.* **85**, 5214–5217 (2000).
26. Ferrari, A. C. et al. Raman spectrum of graphene and graphene layers. *Phys. Rev. Lett.* **97**, 187401 (2006).
27. Lee, J. E., Ahn, G., Shim, J., Lee, Y. S. & Ryu, S. Optical separation of mechanical strain from charge doping in graphene. *Nat. Commun.* **3**, 1024 (2012).
28. Zabel, J. et al. Raman spectroscopy of graphene and bilayer under biaxial strain: bubbles and balloons. *Nano Lett.* **12**, 617–621 (2012).
29. Neumann, C. et al. Raman spectroscopy as probe of nanometre-scale strain variations in graphene. *Nat. Commun.* **6**, 8429 (2015).
30. Piscanec, S., Lazzeri, M., Mauri, F., Ferrari, A. C. & Robertson, J. Kohn anomalies and electron-phonon interactions in graphite. *Phys. Rev. Lett.* **93**, 185503 (2004).
31. Lazzeri, M. & Mauri, F. Nonadiabatic Kohn anomaly in a doped graphene monolayer. *Phys. Rev. Lett.* **97**, 266407 (2006).
32. Pisana, S. et al. Breakdown of the adiabatic Born–Oppenheimer approximation in graphene. *Nat. Mater.* **6**, 198–201 (2007).
33. .Charlier, J.-C., Eklund, P. C., Zhu, J. & Ferrari, A. C. in *Carbon Nanotubes* (eds Jorio, A. et. al) 673–709 (Springer, 2008).
34. Das, A. et al. Phonon renormalization in doped bilayer graphene. *Phys. Rev. B* **79**, 155417 (2009).
35. Ribeiro, H. B. et al. Origin of van Hove singularities in twisted bilayer graphene. *Carbon* **90**, 138–145 (2015).
36. Lazzeri, M., Piscanec, S., Mauri, F., Ferrari, A. C. & Robertson, J. Phonon linewidths and electron-phonon coupling in graphite and nanotubes. *Phys. Rev. B* **73**, 155426 (2006).
37. Efthimiopoulos, I., Mayanna, S., Stavrou, E., Torode, A. & Wang, Y. Extracting the anharmonic properties of the G-band in graphene nanoplatelets. *J. Phys. Chem. C* **124**, 4835–4842 (2020).
38. Sharpe, A. L. et al. Emergent ferromagnetism near three-quarters filling in twisted bilayer graphene. *Science* **365**, 605–608 (2019).
39. Serlin, M. et al. Intrinsic quantized anomalous hall effect in a moiré heterostructure. *Science* **367**, 900–903 (2020).
40. Polshyn, H. et al. Large linear-in-temperature resistivity in twisted bilayer graphene. *Nat. Phys.* **15**, 1011–1016 (2019).

Methods

Theory

Phonons are computed using a combination of a second-generation REBO potential for intralayer interactions and the registry-dependent Kolmogorov–Crespi potential, in its local normal formulation for interlayer interactions, as fully described in ref. [6]. For rTBG, relaxation of the structure in an energy-minimum microstate is crucial for an accurate description of its properties, and here all atomic positions and lattice parameters of the considered structures are optimized until all force components are less than 10^{-3} eV per atom. The dynamical force constants at the zone centre are computed using finite differences. While our method is able to investigate (and unfold) phonons in rTBG structures made of tens of thousands of atoms, we are not able to reach structures with twist angles smaller than $\theta \approx 0.9°$, as the system size becomes prohibitively large in terms of diagonalization of the dynamical matrix, impinging affordable cost to computer memory, rather than CPU time.

The electronic structure is computed by diagonalizing a tight-binding Hamiltonian based on the recursive Green's function, allowing us to compute highly accurate electronic models (that is, atomistic tight-binding Hamiltonians taking into account the effects of structural relaxation), which enables computation of the real-space and momentum-dependent local density of electronic states LDOS(E, $\mathbf{r}$, $\mathbf{k}$) of rTBG with extremely small angles (that is, large moiré superlattices). This efficient numerical technique allows us to calculate both local and total DOS using the same data from the fully relaxed structure used for phonon calculations, and to present the electronic structure of rTBG using real- or momentum-space maps, delivering results that are not obtainable with continuous models. More details are provided in Supplementary Information.

Optical setup

The nano-Raman system is a combination of a micro-Raman and a scanning probe microscopy (SPM) setup in a tip-enhanced Raman spectroscopy (TERS) configuration, as described in ref. [41], where the radially polarized light reaches the sample and the tip coming from an inverted optical microscope (thus limited to transparent substrates[42]), tightly focused by an oil-immersion objective (1.4 numerical aperture), and the back-scattered light is collected by a spectrometer equipped with a charge-coupled device (CCD). The TERS tips used are monopole-based plasmon-tunable tip pyramids, with a nanopyramid size of $L = 470$ nm, which is resonant with the HeNe excitation laser (633 nm), generating an unusually high local enhancement, enough to substantially surpass the Raman signal coming from the considerably larger confocal illumination area[43]. This nano-antenna was produced as described in ref. [22], with an apex diameter of 10 nm, as measured by scanning electron microscopy, generating a TERS resolution of the order of 20 nm, as observed in our data. The experiments are conducted under ambient conditions, with the excitation laser power limited to 0.15 mW to avoid TERS tip burning and accumulation times limited to 0.5 s per spectrum to avoid too long hyperspectral TERS acquisitions.

Sample preparation procedure and characterization

Clean rTBG samples without a top, capping hBN flake, deposited on a glass coverslip are needed for the high-quality nano-Raman data. To produce such samples, we developed a dry tear-and-stack method, using a polydimethylsiloxane (PDMS) semi-pyramidal stamp covered with a polycarbonate sheet (Extended Data Fig. 5). The method is similar to the standard tear-and-stack[44], but we use the PDMS stamp to tear a graphene flake in two pieces and stack them together, forming the rTBG arrangement. Next, we dry-transfer the rTBG from the stamp to an hBN flake, a flat substrate that is sufficiently decoupled from the sample[45], thus avoiding vibrational interference, reducing the surface roughness and improving the cleanliness of the sample. We do not heat the polycarbonate in this process to avoid contamination residues, we just make physical contact between the rTBG and hBN flakes, thus obtaining clean TBG without further sample annealing. See Supplementary Fig. 1 for more details.

These samples were also characterized extensively using SPM, including atomic force microscopy (AFM; Extended Data Fig. 6), scanning microwave impedance microscopy (sMIM; Extended Data Fig. 7) and scanning tunnelling microscopy (not shown).

Data analysis

While the images in Fig. 1d, e were built directly from the spectral G′-band intensity and the G-band linewidth, the AA and SP images in Fig. 2d, e relied on principal component analysis, owing to the low signal-to-noise ratio observed for these weak features. Principal component analysis generated the representative features displayed in Fig. 2f, g, and each spectrum of the corresponding hyperspectral data was fitted with a linear combination of the representative features. The fitted spectrum was confirmed to properly represent the feature signature by computing the Pearson's correlation between the raw data and the fitted profile. The contribution plot in Fig. 2d, e is defined by the percentile values of these linear coefficients. The contribution in Fig. 3c, d follows the same definition with respect to the spectral features in Fig. 3a, b.

Data availability

The experimental data related to this work, including the raw and processed data, are available at https://doi.org/10.5281/zenodo.4313869. The data related to the theoretical work are available on request to the corresponding authors.

41. Rabelo, C., Miranda, H., Vasconcelos, T. L., Cancado, L. G. & Jorio, A. Tip-enhanced Raman spectroscopy of graphene. In *4th Int. Symp. Instrumentation Systems, Circuits and Transducers (INSCIT)* 1–6 (IEEE, 2019).
42. Miranda, H. et al. Impact of substrate on tip-enhanced Raman spectroscopy: a comparison between field-distribution simulations and graphene measurements. *Phys. Rev. Res.* **2**, 023408 (2020).
43. Miranda, H. et al. Optical properties of plasmon-tunable tip pyramids for tip-enhanced raman spectroscopy. *Phys. Status Solidi* **14**, 2000212 (2020).
44. Kim, K. et al. van der Waals heterostructures with high accuracy rotational alignment. *Nano Lett.* **16**, 1989–1995 (2016).
45. Woods, C. R. et al. Commensurate–incommensurate transition in graphene on hexagonal boron nitride. *Nat. Phys.* **10**, 451–456 (2014).
46. Pizzocchero, F. et al. The hot pick-up technique for batch assembly of van der Waals heterostructures. *Nat. Commun.* **7**, 11894 (2016).

Acknowledgements This work was supported by CNPq (302775/2018-8 and INCT/Nanomaterials de Carbono), CAPES (RELAII and 88881.198744/2018-01) and FAPEMIG, Brazil. V.-H.N. and J.-C.C. acknowledge financial support from the Fédération Wallonie-Bruxelles through the ARC on 3D nano-architecturing of 2D crystals (16/21-077), from the European Union's Horizon 2020 Research Project and Innovation Program — Graphene Flagship Core3 (881603), from the Flag-Era JTC projects 'MECHANIC' (R.50.07.18) and 'TATTOOS' (R.8010.19), from the Belgium FNRS through the research projects T.1077.15 and T.0051.18, and from the Francqui-Stichting Foundation. V.M. and M.L. acknowledge support from NY State Empire State Development's Division of Science, Technology and Innovation (NYSTAR).

Author contributions Sample preparation: A.C.G., D.M., F.C.S., E.G.S.N., J.S.L., L.C.C., R.N. and V.O.; K.W. and T.T. provided hBN crystals. Nano-Raman measurements: A.C.G., C.R. and T.L.V. Micro-Raman measurements: A.C.G., E.G.S.N., J.S.L. and R.N. Scanning probe microscopy measurements: D.A.A.O. and G.M.-R. Phonon structure computation: B.v.T., M.L. and V.M. Electronic structure computation: D.P., V.-H.N. and J.-C.C. Data analysis: A.J., A.C.G., C.R., E.G.S.N. and J.L.C. Project idealization and guidance: A.J., G.M.-R., L.G.C., L.C.C. and V.M. Paper writing: A.J., A.C.G. and V.M. Some authors contributed to parts of the text and figures. All authors read and agreed on the final version of the manuscript.

Competing interests The authors declare no competing interests.

Additional information

Supplementary information The online version contains supplementary material available at https://doi.org/10.1038/s41586-021-03252-5.

Correspondence and requests for materials should be addressed to V.M. or A.J.

Peer review information *Nature* thanks Ludger Wirtz and the other, anonymous, reviewer(s) for their contribution to the peer review of this work. Peer reviewer reports are available.

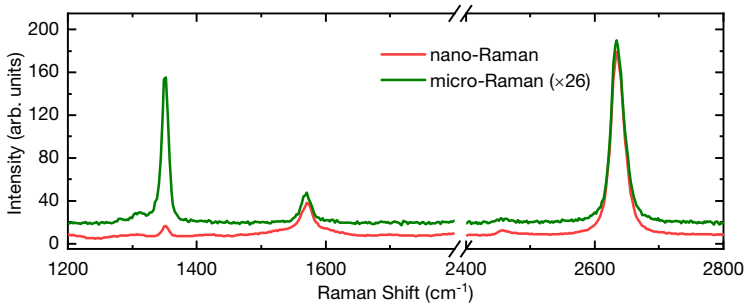

Extended Data Fig. 1 | Comparison between micro- and nano-Raman spectra in the rTBG sample. This figure is a reproduction of Fig. 1c, but with the intensity of the micro-Raman spectrum multiplied by 26 to better visualize and compare the details of the two spectra. The enhancement of the hBN substrate peak is considerably lower, owing to the presence of the graphene sample between the tip and the substrate.

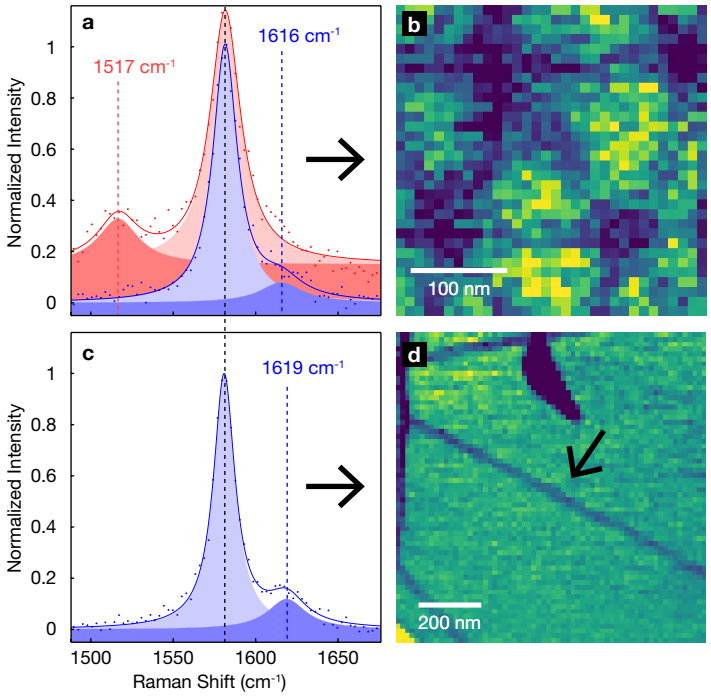

Extended Data Fig. 2 | Representative spectral profiles and images for two other rTBG samples. a, **c**, The spectral Raman profiles evidence different frequency values for the G_r^- and G_r^+ peaks observed in two different rTBG samples (black arrows link the profiles to the corresponding images in **b** and **d**). The vertical lines indicate the central frequencies for the observed G_r^-, G and G_r^+ peaks. **b**, **d**, The spectral images are based on the G′-band intensities (colour scale). The arrow in **d** indicates the where the specrum in **c** was taken. In Fig. 2f (rTBG with $\theta = 0.09°$), the peaks are observed at $\omega_{G_r^-} = 1,522$ cm^{-1} and $\omega_{G_r^+} = 1,612$ cm^{-1}. The frequency difference between the theoretically predicted G_r^- and G_r^+ peaks is $\Delta\omega_{G_r^\pm} = 45$ cm^{-1} (for $\theta = 0.987°$; already reaching the limit of our computational capability). For the experimentally observed G_r^- and G_r^+ peaks for $\theta = 0.09°$, it is $\Delta\omega_{G_r^\pm} = 90$ cm^{-1}. Our ability to experimentally define the θ dependence of the splitting is also limited, by the TERS resolution. We cannot properly image a moiré pattern smaller than 40 nm (twice the TERS resolution), limiting the rTBG samples that we can image to those with $\theta < 0.3°$. The $\Delta\omega_{G_r^\pm}$ splitting is predicted to increase with decreasing twist angle[6], consistent with experimental observations: for $L_M \approx 160$ nm ($\theta \approx 0.09°$), we observed $\omega_{G_r^-} = 1,522$ cm^{-1} and $\omega_{G_r^+} = 1,612$ cm^{-1} ($\Delta\omega_{G_r^\pm} = 90$ cm^{-1}); for $L_M \approx 210$ nm ($\theta \approx 0.07°$), we observed $\omega_{G_r^-} = 1,517$ cm^{-1} and $\omega_{G_r^+} = 1,616$ cm^{-1} ($\Delta\omega_{G_r^\pm} = 99$ cm^{-1}); for $L_M > 1,000$ nm ($\theta < 0.01$), $\omega_{G_r^-}$ was not observed, but $\omega_{G_r^+} = 1,619$ cm^{-1} follows the trend.

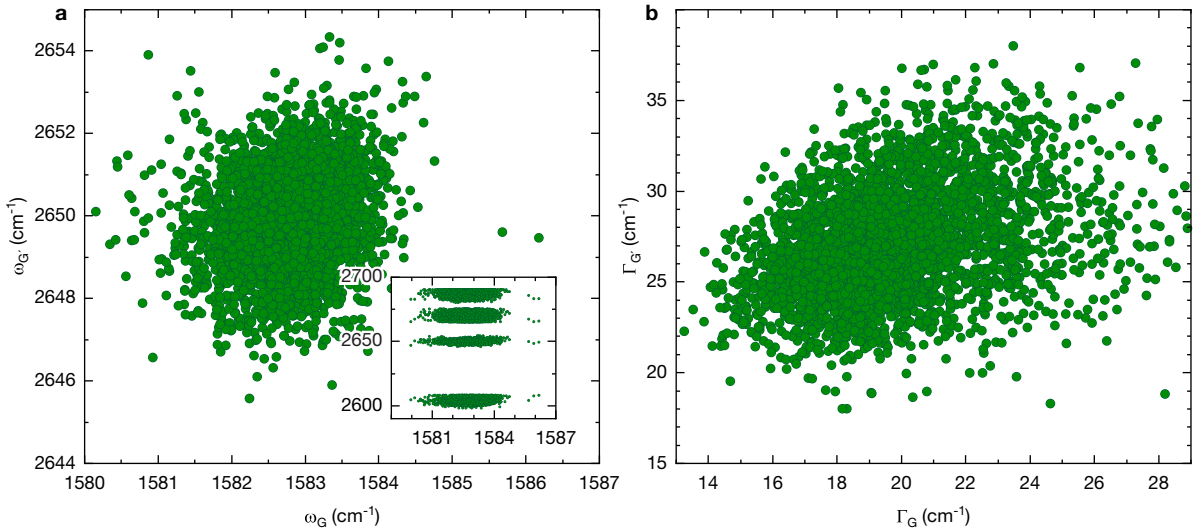

Extended Data Fig. 3 | Correlation between G- and G′-band frequencies and FWHMs. a, **b**, The frequencies (**a**) and FWHMs (**b**) are shown for the data displayed in Fig. 1d. The G′ spectra were fitted using four Lorentzians, as per ref. [26]. The results shown here are for the most intense G′ feature (named 'L02' in ref. [26]). The inset in **a** shows the behaviour of the four peaks.

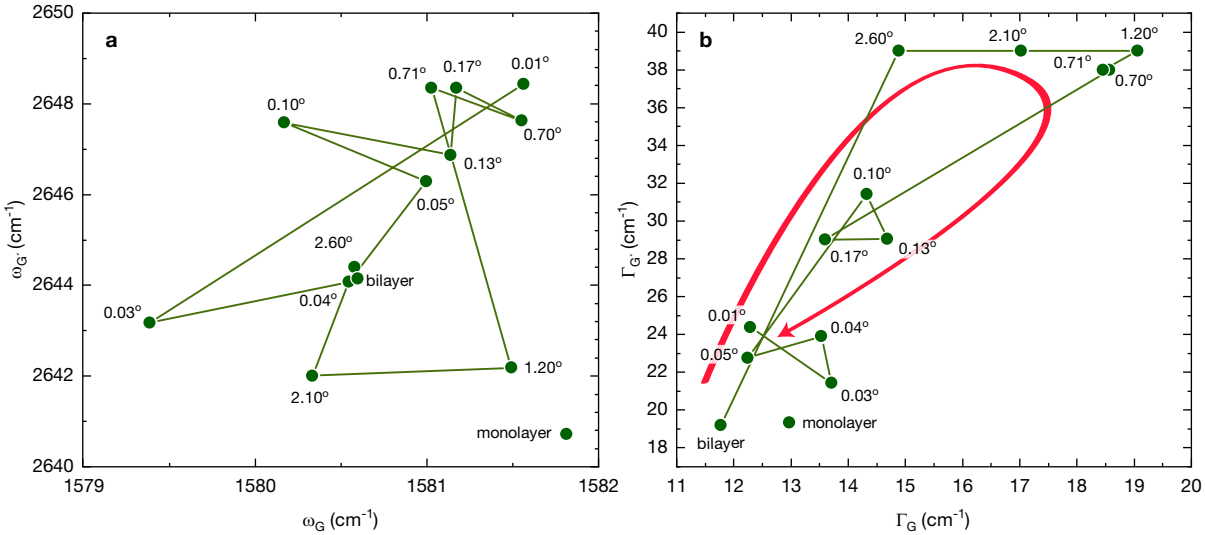

Extended Data Fig. 4 | Correlation between G- and G′-band frequencies and FWHMs. a, **b**, The frequencies (**a**) and FWHMs (**b**) are shown for the data displayed in Fig. 4. The twist angle for each point is labelled. The red curved arrow in **b** indicates a maximum in FWHM observed near the magic angle.

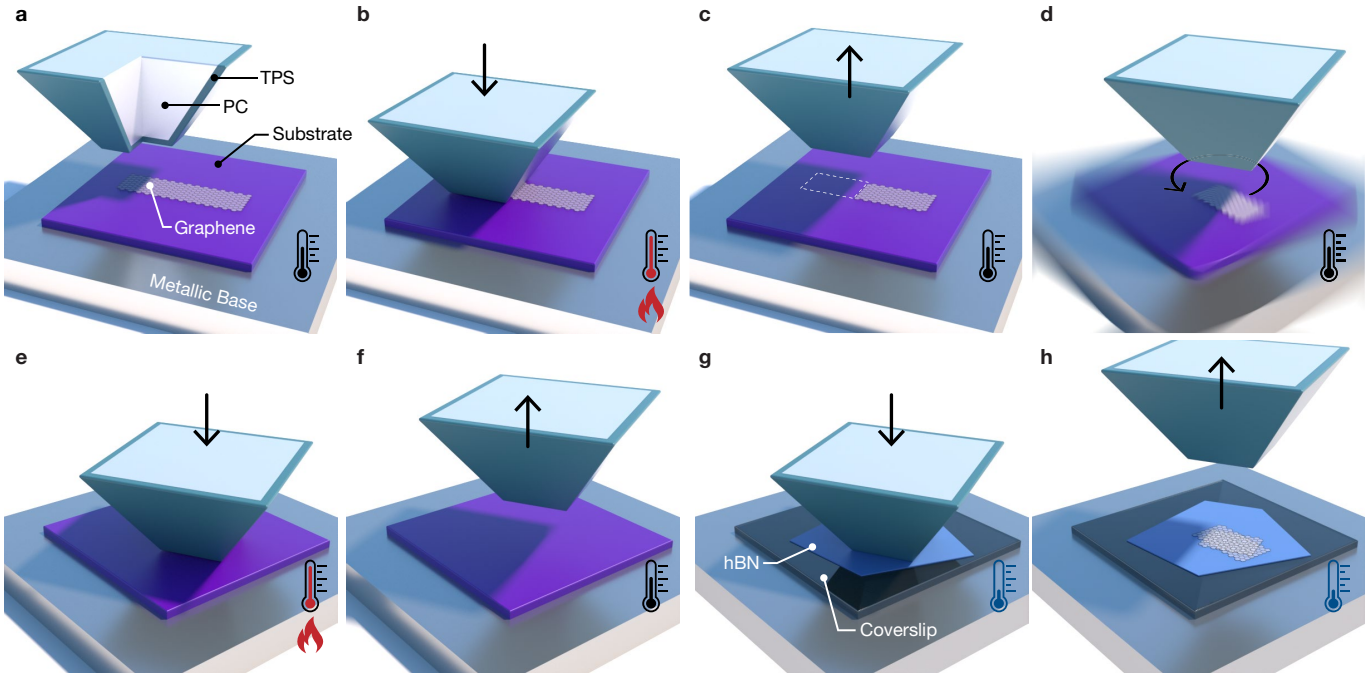

Extended Data Fig. 5 | Schematics of the sample preparation procedure. **a**, We cover the newly developed PDMS tear-and-stack pyramid stamp (TPS) with a polycarbonate (PC) sheet and align the TPS edge with the middle of a graphene flake. **b**, Next, we make contact between the TPS and graphene, followed by a temperature ramp from 70 °C to 80 °C. **c**, We then wait for the system to cool down, reaching a temperature of 70 °C, similarly to the pick-up method[46], removing a piece of the graphene flake. **d**, **e**, We then rotate the base (**d**) and stack the two parts of graphene together, forming the TBG (**e**). **f**, We do the previous temperature ramp and cool-down procedure again to remove the remaining graphene piece. **g**, Next, we put the TBG in contact with a flat and clean hBN flake at room temperature. **h**, The van der Waals interactions between them is strong enough for the hBN to pull out the TBG from the TPS.

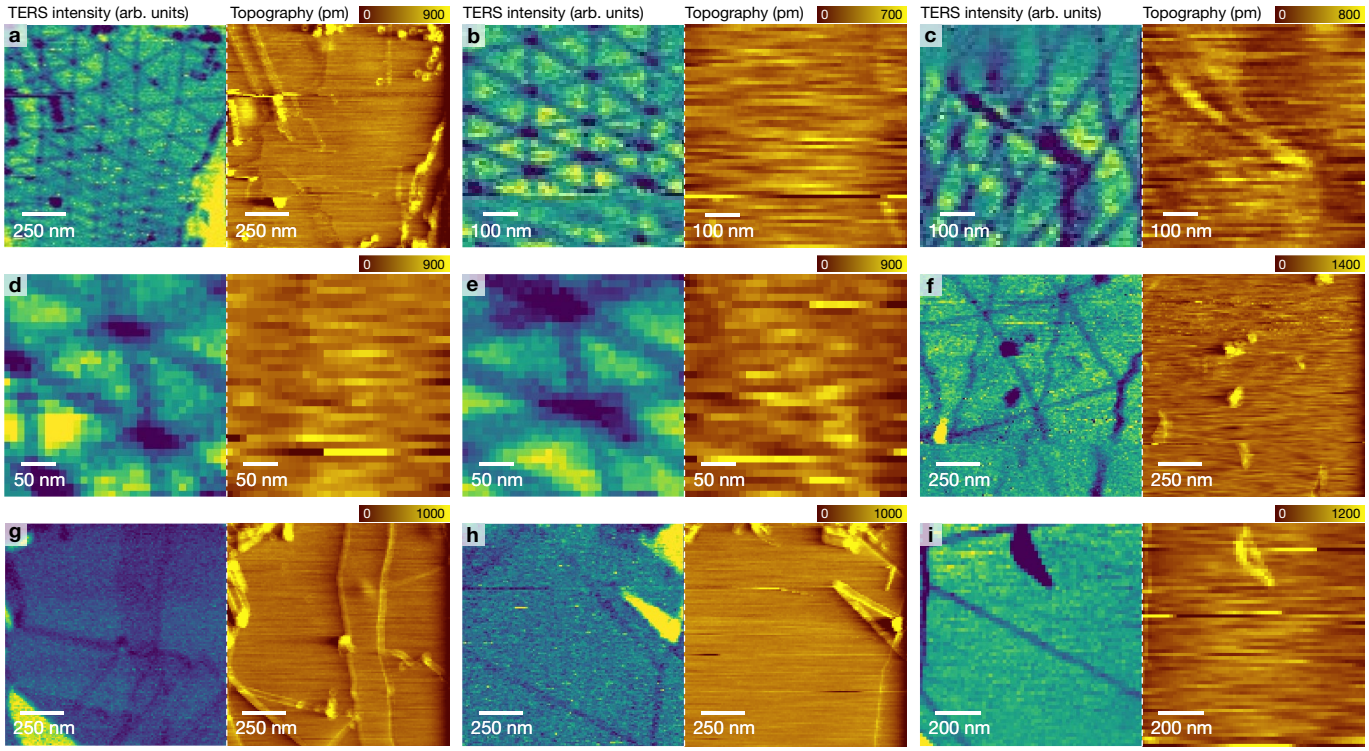

Extended Data Fig. 6 | TERS imaging of nine different moiré structures from rTBG. a–i, TERS images from various moiré structural formations based on the G′-band intensity (left) and the simultaneously obtained AFM images (right). The solitonic structures are observable only in the TERS images (darker blue lines); they are absent in the AFM images. The contrast discontinuities in **b** and **f** are due to the realignment of the tip with the laser during the scan.

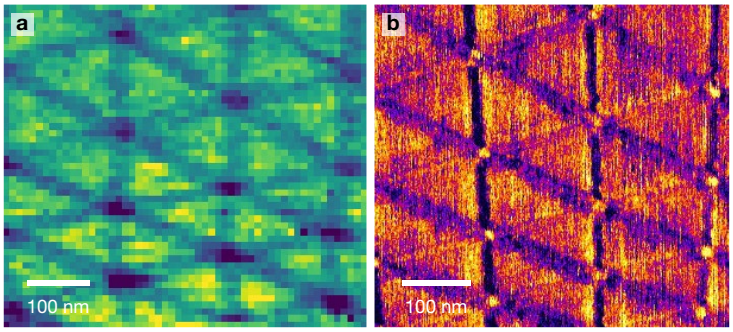

Extended Data Fig. 7 | Multi-technique structural characterization of rTBG. a, **b**, TERS (**a**) and sMIM (**b**) images of the same rTBG region.